


# Novel Bayesian probability method in predictions of nuclear masses

Jiaze Xie,<sup>\*</sup> Keping Wang,<sup>\*</sup> Chuan Wang, Wanqing Gao, Min Ju<sup>✉</sup>, and Jian Liu<sup>✉†</sup>  
*College of Science, China University of Petroleum (East China), Qingdao 266580, China*

 (Received 10 November 2023; revised 27 March 2024; accepted 28 May 2024; published 20 June 2024)

Machine learning methods have recently gained interest in the complexity of nuclear mass prediction. According to previous studies, we propose a continuous Bayesian probability (CBP) classifier combined with Bayesian model averaging (BMA) to refine the descriptions of sophisticated nuclear mass models. In the CBP method, the nuclear masses are considered continuous variables to generate prior and conditional probability density functions (PDFs), and the posterior PDFs are determined by the Bayesian formula. The global optimizations and the extrapolating analyses exhibit impressive improvements. Additionally, we employ the BMA method to consider the predictions of different models by assigning weights based on their predictive effectiveness for seven benchmark nuclei. By presenting predictions of the neutron drip line, we assess the reliability of the refinements of the BMA method. The methods proposed in this paper provide an effective way of predicting the nuclear mass in unknown regions and can be applied to other model-based extrapolations of nuclear properties.

DOI: [10.1103/PhysRevC.109.064317](https://doi.org/10.1103/PhysRevC.109.064317)

## I. INTRODUCTION

The accurate calculation of nuclear masses is important for nuclear physics and other fields. Researches on nuclear masses can not only guide theoretical studies for nuclear structure [1–4], but also help in understanding nuclear decays [5–9], nuclear synthesis [10,11], and nuclear astrophysics [12,13]. There are mainly two types of experimental methods for measuring nuclear masses. The first employs nuclear mass spectrometry, which relies on determining the time-of-flight or cyclotron frequency of nuclei [14–17]. The second is through analyzing the  $Q$  values of nuclear reactions or decays to extract nuclear masses [18,19].

Measurements of nuclear masses have achieved great progress in recent years. However, out of the approximately 7000 nuclei, only roughly 3500 have experimental mass values [20–22]. Therefore, several theoretical models have been proposed to provide the missing information. Nuclear mass models can be generally divided into two categories. One is the microscopic nuclear structure models with parameter sets, such as the Hartree-Fock-Bogoliubov (HFB) models [23–28] (e.g., Skyrme-Pairing (SkP) [29], Skyrme-Lyon 4 (SLy4) [30]) and the relativistic mean-field (RMF) models [31–38] (e.g., Indian University–Florida State University (IU-FSU) [39], Non-Linear 3\* (NL3\*) [40], Non-Linear Sigma-Hyperon (NLSH) [41], and Tyle-Miller 1 (TM1) [42]). The other is semiempirical formulas (e.g., Weizsäcker-Skyrme (WS\*) [43,44], Duflo-Zuker (DZ) [45,46], and the finite-range droplet model (FRDM) [47,48]). Although the theoretical mass models are successful in describing the changing rule of nuclear masses, many researches

still require higher precision, such as the synthesis of super-heavy nuclei [10,11].

It is difficult to increase the accuracy of predictions for nuclear masses based on theoretical models due to the large amount of computation and the complexity of the interaction. Therefore, machine learning has been introduced as a vital tool in the field of nuclear mass systematics [49–56]. Based on the machine learning method, the predictions of nuclear masses and neutron drip lines have exhibited impressive improvements [57,58]. The machine learning models can be broadly divided into two major classifications: generative models and discriminative models. Generative models generate new examples by modeling the joint probability distribution of data using, e.g., the Gaussian process (GP) [59–61] or the naive Bayesian probability (NBP) classifier [62,63]. Discriminative models classify data into different categories by directly modeling the conditional probability distribution using, e.g., a decision tree (DT) [64], a support vector machine (SVM) [65], or a neural network (NN) [66,67]. The choice of algorithm depends on the properties of the dataset. For few training data, generative models can be more suitable because they attempt to model the full distribution of the data, potentially capturing more information [68,69]. For example, the NBP method, as a generative model, has been proposed to improve the predictions of nuclear masses and radii from theoretical models [62,63].

Based on the naive Bayesian probability (NBP) classifier, a continuous Bayesian probability (CBP) classifier is put forward to improve the description of the nuclear mass. In the framework of CBP, the deviations of mass between experimental data and theoretical results, namely the mass residuals  $\delta$ , are considered continuous variables to guarantee the contributions of all experimental data. By applying the Bayesian formula, we calculate the posterior probability density function (PDF) of residuals to obtain the estimated

<sup>\*</sup>These authors contributed equally to this work.

<sup>†</sup>Contact author: liujian@upc.edu.cn

residual. To further improve the accuracy of predictions by the CBP method, we employ the Bayesian model average (BMA) method to consider the results of different models comprehensively. The BMA method is a way to estimate the predictive performance of various theoretical models and averages the results according to the effectiveness of individual model [70], and has been adopted to provide quantified predictions in nuclear studies [59–61].

In this paper, we utilize the CBP method on three classes of theoretical nuclear models, which include the HFB model, the RMF model, and the semiempirical formulas. The properties of the CBP method are systematically analyzed through global optimization and extrapolation. For the global optimizations, the entire data set consists of 3471 experimental masses of nuclei with  $Z \geq 8$  in the Atomic Mass Evaluation of 2020 (AME2020) [71]. For the extrapolations, the learning set consists of 3007 nuclei that occurred in the AME2003 [72], while the validation set includes 464 nuclei newly added in the AME2020. After the refinement of the CBP method, the BMA method is applied to assign weights to different theoretical models. The weights are determined according to the predictive results of seven benchmark nuclei:  $^{19}\text{Mg}$ ,  $^{54}\text{Sc}$ ,  $^{67}\text{Kr}$ ,  $^{80}\text{Zr}$ ,  $^{112}\text{Mo}$ ,  $^{127}\text{La}$ , and  $^{153}\text{Pm}$ , as published in Refs. [4, 73–78]. In addition, we display the extrapolations of the neutron drip line for Ca isotopes outside of the AME compilation by a graphic depiction. Our results illustrate that the CBP method combined with the BMA method can effectively improve the description of nuclear mass, and can be applied to predict nuclei in unknown regions of the nuclear chart.

This paper is structured as follows: In Sec. II, we provide detailed discussions of the theoretical frameworks of the CBP and BMA methods. In Sec. III, we discuss the numerical outcomes and provide corresponding discussions. Finally, a brief conclusion is provided in Sec. IV.

## II. FRAMEWORK

This section presents the CBP framework and BMA theory. In the CBP framework, mass residuals are considered continuous variables, and the Bayesian formula is used to calculate the posterior PDFs of residuals for the predicted nucleus. The estimated residual can be obtained from these PDFs. In the BMA framework, the method of assigning different model weights is introduced under the Bayesian theorem, and these weights can be used to propose the formula for the average mass result. Furthermore, the precision and uncertainty assessment standards are presented in this paper.

### A. The continuous Bayesian probability method

The Bayesian theorem is an effective approach to describing the posterior probability of a numeric target value  $Y$  based on a sample set  $X$ . For continuous random variables  $X$ , the multivariate Bayesian theorem for calculating the posterior PDF can be expressed as

$$p(Y|X) = \frac{p(X_1|Y)p(X_2|Y) \cdots p(X_m|Y)p(Y)}{\int p(X_1|Y)p(X_2|Y) \cdots p(X_m|Y)p(Y)dY}, \quad (1)$$

where  $p(X_i|Y)$  is the conditional PDF, which represents the probability of events  $X_i$  happening under the assumption of events  $Y$ .  $p(Y)$  is the prior PDF, which denotes the occurrence frequencies of certain  $Y$ .

Given that the nuclear mass residuals are continuous variables, Eq. (1) is utilized in refining the description of nuclear mass from the theoretical models. The event  $Y$  refers to the mass residual  $\delta$ , which is a continuous random variable. The events  $X_i$  refer to the proton number  $Z_i$  and neutron number  $N_i$ . Assuming that  $Z_i$  and  $N_i$  are independent of others, the posterior PDF  $p(\delta|Z_i, N_i)$  can be given by

$$p(\delta|Z_i, N_i) = \frac{p(Z_i|\delta)p(N_i|\delta)p(\delta)}{\int p(Z_i|\delta)p(N_i|\delta)p(\delta)d\delta}. \quad (2)$$

The conditional PDFs  $p(Z_i|\delta)$  and  $p(N_i|\delta)$  in Eq. (2) are estimated using the univariate Bayesian theorem,

$$p(Z_i|\delta) = \frac{p(\delta|Z_i)p(Z_i)}{p(\delta)}, \quad (3)$$

$$p(N_i|\delta) = \frac{p(\delta|N_i)p(N_i)}{p(\delta)}. \quad (4)$$

In Eqs. (3) and (4), the prior probability  $p(Z_i(N_i))$  represents the frequency of  $Z_i$  or  $N_i$  occurring in the training set. The likelihood PDF  $p(\delta|Z_i)$  and  $p(\delta|N_i)$  can be evaluated by the kernel density estimator (KDE),

$$p(\delta|Z_i) = \frac{1}{n_Z h_Z} \sum_{i=1}^{n_Z} K\left(\frac{\delta - \delta_i}{h_Z}\right), \quad (5)$$

$$p(\delta|N_i) = \frac{1}{n_N h_N} \sum_{i=1}^{n_N} K\left(\frac{\delta - \delta_i}{h_N}\right), \quad (6)$$

where  $K(t) = (2\pi)^{-1/2} e^{-t^2/2}$ . The kernel width  $h_Z(h_N)$  is a pending parameter.  $n_Z(n_N)$  represents the number of nuclei with  $Z_i(N_i)$ . Similarly, the prior PDF  $p(\delta)$  in Eqs. (2)–(4) can also be calculated using KDE with the kernel width  $h_\delta$ ,

$$p(\delta) = \frac{1}{n h_\delta} \sum_{i=1}^n K\left(\frac{\delta - \delta_i}{h_\delta}\right), \quad (7)$$

where  $n$  is the number of all the nuclei in the training set. In Eqs. (5)–(7), the individual mass residual is  $\delta_i = E_i^{\text{exp}} - E_i^{\text{th}}$ , and the pending parameters  $h_\delta$ ,  $h_Z$ , and  $h_N$  are related to the range of the continuous mass residual  $\delta$ .

In order to incorporate the local relationship between the adjacent nuclei, a weight function is introduced in calculating the likelihood PDF and the prior PDF:

$$w(Z, N; Z_i, N_i) = \exp\left[-\frac{(Z - Z_i)^2 + (N - N_i)^2}{\rho}\right] + \varepsilon, \quad (8)$$

with two parameters  $\rho$  and  $\varepsilon$ .  $\rho$  closely influences the accuracy of prediction and the distance of extrapolation about nuclei, which is set to  $\rho = 2$  in this paper.  $\varepsilon$  affects the posterior PDF stability, and we use  $\varepsilon = 10^{-10}$  to ensure a Gaussian distribution  $p(\delta|Z_i, N_i)$  with independent variable  $\delta$  in this paper. Then the prior PDF  $p(\delta)$  and the likelihood PDF  $p(\delta|Z_i(N_i))$

are transformed into  $p_{\text{wt}}(\delta)$  and  $p_{\text{wt}}(\delta|Z_t(N_t))$ :

$$p_{\text{wt}}(\delta) = \frac{1}{nh_\delta} \sum_{i=1}^n K\left(\frac{\delta - \delta_i}{h_\delta}\right) w(Z_i, N_i; Z_t, N_t), \quad (9)$$

$$p_{\text{wt}}(\delta|Z_t) = \frac{1}{n_Z h_Z} \sum_{i=1}^{n_Z} K\left(\frac{\delta - \delta_i}{h_Z}\right) w(Z_i, N_i; Z_t, N_t), \quad (10)$$

$$p_{\text{wt}}(\delta|N_t) = \frac{1}{n_N h_N} \sum_{i=1}^{n_N} K\left(\frac{\delta - \delta_i}{h_N}\right) w(Z_i, N_i; Z_t, N_t). \quad (11)$$

By combining Eqs. (2)–(11), the posterior PDF  $p(\delta|Z_t, N_t)$  can be calculated and the final refined residual of the target nucleus can be obtained by computing the expectation value

$$\delta^{\text{em}}(Z, N) = \int \delta p(\delta|Z, N) d\delta. \quad (12)$$

Finally, the refined residual is added to the theoretical mass value  $E^{\text{th}}(Z, N)$  to get the final corrected mass prediction  $E^{\text{corr}}(Z, N)$ ,

$$E^{\text{corr}}(Z, N) = E^{\text{th}}(Z, N) + \delta^{\text{em}}(Z, N). \quad (13)$$

### B. Bayesian model averaging

In order to combine the advantages of different theoretical models and comprehensively consider the predictive performance of each theoretical model, we introduced the BMA method on the basis of the CBP method. The BMA method is an optimized algorithm for selecting the appropriate description from a set of candidates. In this paper, nine theoretical models are employed to obtain the residuals, including the nonrelativistic HFB models, the relativistic RMF models, and the semiempirical formulas. The inclusion of multiple models can lead to variations in predicted results. To determine the appropriate weights for each model, we utilize the BMA method based on the predictive performance of the target nuclear. Given a set of  $K$  candidate models  $M_1, \dots, M_K$ , the Bayesian theorem can be used to determine the weight assigned to each model,

$$P(M_k|D) = \frac{P(D|M_k)P(M_k)}{\sum_{i=1}^K P(D|M_i)P(M_i)}. \quad (14)$$

In this study, the data set  $D$  contains seven benchmark nuclei,  $^{19}\text{Mg}$ ,  $^{54}\text{Sc}$ ,  $^{67}\text{Kr}$ ,  $^{80}\text{Zr}$ ,  $^{112}\text{Mo}$ ,  $^{127}\text{La}$ , and  $^{153}\text{Pm}$ , as established in Refs. [4, 73–78], which are utilized to evaluate the accuracy of models based on the entire nuclide chart. The prior probability  $P(M_k) = \frac{1}{K}$  is related to the number of candidate models, while the conditional probability  $P(D|M_k)$  is determined by the predictive outcomes of each theoretical model  $M_k$ ,

$$P(D|M_k) = \prod_j \frac{1}{\sqrt{2\pi}} \exp\left[-\frac{(\delta_j^{\text{corr}})^2}{2}\right], \quad (15)$$

where  $\delta_j^{\text{corr}} = E_j^{\text{exp}} - E_j^{\text{corr}}$  are the refined residuals of benchmark nuclei of the corresponding theoretical model  $M_k$ .

Finally, the average mass result  $\bar{E}(Z_t, N_t)$  by BMA for nucleus  $(Z_t, N_t)$  can be obtained by

$$\bar{E}(Z_t, N_t) = \sum_{i=1}^K E_i^{\text{corr}} P(M_i|D). \quad (16)$$

### C. Assessment standards and uncertainties

The assessment standards for the predicted results and the corresponding uncertainties are presented as follows. Numerous methodologies are available for evaluating the performance of a predictive model. In this paper, we utilize the standard deviation  $\sigma_{\text{rms}}$  to measure the biases between the corrected theoretical results and experimental data for a given model, which is defined as

$$\sigma_{\text{rms}}^2 = \frac{1}{n} \sum_{i=1}^n (E_i^{\text{corr}} - E_i^{\text{exp}})^2. \quad (17)$$

Selecting distinct evaluation methods will result in discrepant deviation data. Different from Eq. (17), the maximum-likelihood method is applied to obtain the intrinsic model error in Ref. [47], which provides an error of 0.56 MeV for the FRDM model.

In the CBP method, the uncertainties of predictions are derived from the posterior PDF. The one-sigma uncertainty  $\sigma^{\text{em}}(Z, N)$  of each mass model for the specific nucleus  $(Z, N)$  is defined as

$$\sigma^{\text{em}}(Z, N) = \sqrt{\int [\delta - \delta^{\text{em}}(Z, N)]^2 p(\delta|Z, N) d\delta}, \quad (18)$$

and the uncertainty of BMA is given by

$$\sigma^{\text{BMA}}(Z, N) = \sum_{i=1}^K \sigma_i^{\text{em}} P(M_i|D). \quad (19)$$

## III. RESULTS

In this section, the CBP and BMA methods are utilized to refine the theoretical nuclear masses. The raw results are calculated using the nonrelativistic HFB models, the relativistic RMF models, and semiempirical formulas. Then we analyze the global optimizations of the CBP method and assess its extrapolating capabilities. Subsequently, the nuclear masses of different models based on benchmark nuclei are refined through the BMA method.

### A. Global optimizations of the CBP method

The global optimizations of the CBP method are first analyzed. The entire set consists of 3471 nuclei with  $Z \geq 8$ , as reported in AME2020. We calculate the theoretical binding energies for each nucleus with nine mass models, including HFB models with SkP and SLy4 parameter sets, the RMF models with IU-FSU, NL3\*, NLSH, and TM1 parameter sets, as well as the semiempirical formulas with WS\*, DZ10, and FRDM parameter sets. For deformed HFB models the code and detailed formulas can be found in Ref. [79], while for deformed RMF models they can be found in Ref. [80]. During

TABLE I. The standard deviation  $\sigma_{\text{pre}}$  (MeV) from the theoretical models and  $\sigma_{\text{post}}$  (MeV) after the CBP and NBP refinements. 3471 nuclei in AME2020 with  $Z \geq 8$  are chosen as the entire set.

Methods	Models	HFB		RMF				Semiempirical		
		SkP	SLy4	IU-FSU	NL3*	NLSH	TM1	WS*	DZ10	FRDM
CBP	$\sigma_{\text{pre}}$	4.16	6.01	6.07	2.89	4.15	4.68	0.60	1.25	0.99
	$\sigma_{\text{post}}$	0.49	0.50	1.17	0.96	0.98	1.00	0.24	0.27	0.27
	$\Delta\sigma/\sigma_{\text{pre}}$	88%	92%	81%	67%	77%	79%	59%	78%	72%
NBP	$\sigma_{\text{post}}$	0.70	0.68	1.62	1.23	1.21	1.26	0.32	0.40	0.35
	$\Delta\sigma/\sigma_{\text{pre}}$	83%	89%	73%	57%	71%	73%	47%	68%	64%

RMF calculations, the pairing correlations are incorporated through the BCS method. By comparing the theoretical results with experimental data, the corresponding raw residual  $\delta^{\text{pre}} = E^{\text{exp}} - E^{\text{th}}$  for each nucleus is calculated for each mass model.

After calculating the raw mass residuals  $\delta^{\text{pre}}$ , the CBP method is applied to refine the descriptions of each mass model. The sample set for each target nucleus comprises 3470 nuclei in AME2020, excluding the target nucleus itself. The corresponding prior PDF  $p_{\text{wt}}(\delta)$ ,  $p_{\text{wt}}(Z_t(N_t))$ , and the conditional PDF  $p_{\text{wt}}(Z_t(N_t)|\delta)$  can be calculated with Eqs. (9)–(11). Then, the Bayesian formula (2) gives the posterior PDF  $p_{\text{wt}}(\delta|Z_t, N_t)$ . Finally, Eqs. (12) and (13) are used to obtain the refined mass of each target nucleus. The pending parameters  $h_\delta$ ,  $h_Z$ , and  $h_N$  in Eqs. (9)–(11) reflect the distribution range of raw mass residuals  $\delta^{\text{pre}}$ . In the entire set, most of the  $\delta^{\text{pre}}$  are between 0 and 20 MeV. Selecting the value of  $h_\delta$  within this range can optimize the predictive performance. Similarly, the differences between  $\delta^{\text{pre}}$  of isotopes and isotones are largely within the range of 0 and 5 MeV. We ultimately chose parameters  $h_\delta = 7.00 \text{ MeV}^{-1}$ ,  $h_Z = 2.00 \text{ MeV}^{-1}$ , and  $h_N = 3.00 \text{ MeV}^{-1}$  for all nine theoretical models. Adjusting the three parameters within their corresponding range of  $\delta^{\text{pre}}$  makes a small difference in the predictive results.

Table I presents the performance of the global optimization of the CBP method. The raw deviation  $\sigma_{\text{pre}}$  denotes the standard deviation of the theoretical results from various mass models for a total of 3471 nuclei, while the posterior deviation  $\sigma_{\text{post}}$  is the standard deviation of the corrected results from the CBP method.  $\Delta\sigma/\sigma_{\text{pre}} = (\sigma_{\text{pre}} - \sigma_{\text{post}})/\sigma_{\text{pre}}$  evaluates the effectiveness of the global optimization of the CBP method. For the HFB model with SkP and SLy4 parameter sets, the standard derivations  $\sigma_{\text{post}}$  become about 0.5 MeV after refinements, and the accuracy of the descriptions of the nuclear mass improves by about 90%. For the RMF model with IU-FSU, NL3\*, NLSH, and TM1 parameter sets, the  $\sigma_{\text{post}}$  are improved to around 1 MeV after the CBP method refinements, which show a 70%–80% reduction. For the semiempirical formulas, the CBP method reduces all the  $\sigma_{\text{post}}$  to around 0.2 MeV and exhibits over 60% improvements.

To establish the superiority of the CBP method, we display the outcomes of the NBP method in Table I for comparison. The NBP method is a discrete Bayesian probability approach that employs the *k-means* algorithm to determine cluster centers. Table I shows the posterior deviation  $\sigma_{\text{post}}$  and the  $\Delta\sigma/\sigma_{\text{pre}}$  calculated by the NBP method. For the

three models, there is a 5%–10% enhancement in predictive accuracy concerning nuclear masses in the CBP classifier compared to the NBP classifier. This can be attributed to the continuous PDF employed in the CBP method instead of the discrete probability used in the NBP method. To underscore the enhanced effects of continuous PDF, we conduct an in-depth comparative analysis between the CBP and NBP methods. Fig. 1 exhibits the posterior PDF of  $^{29}\text{Si}$  calculated by CBP and NBP methods. Through *k-means* clustering, the NBP method provides a finite number of mass residuals  $\delta_i$ . The residual with the highest posterior probability is selected as the estimated residual  $\delta^{\text{em}}$ . In contrast, the CBP method considers residuals as continuous variables, and the final refined residual  $\delta^{\text{em}}$  is obtained by integrating over the entire residual distribution space. In comparison with the limited data in the NBP method, the CBP method takes into account the contribution of all possible residuals, hence leading to a higher degree of improvement.

In Table I, one can observe that different types of nuclear mass models show dissimilar  $\sigma_{\text{post}}$ , and the  $\sigma_{\text{post}}$  tend to be consistent for models of the same class regardless of

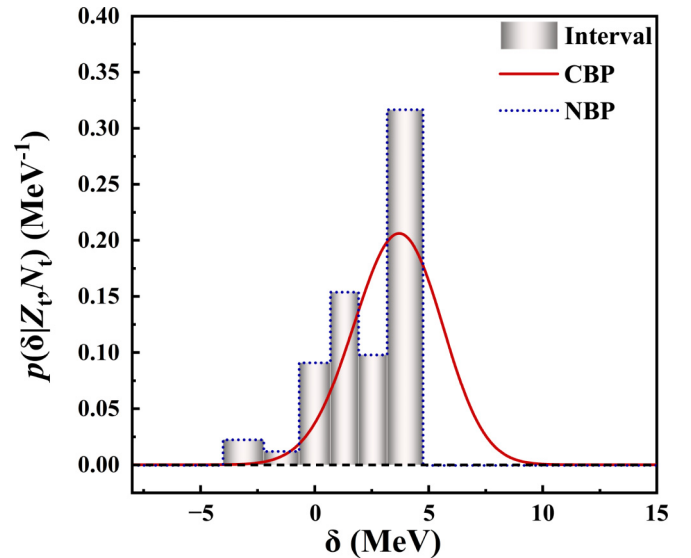


FIG. 1. Posterior probability density for the CBP and NBP methods. The red curve depicts the continuous PDF  $p(\delta|Z_t, N_t)$  generated by the CBP method. The blue dotted line represents the discrete PDF  $p(\delta_i|Z_t, N_t)$  obtained by the NBP method, and the grey section denotes the interval of classification.



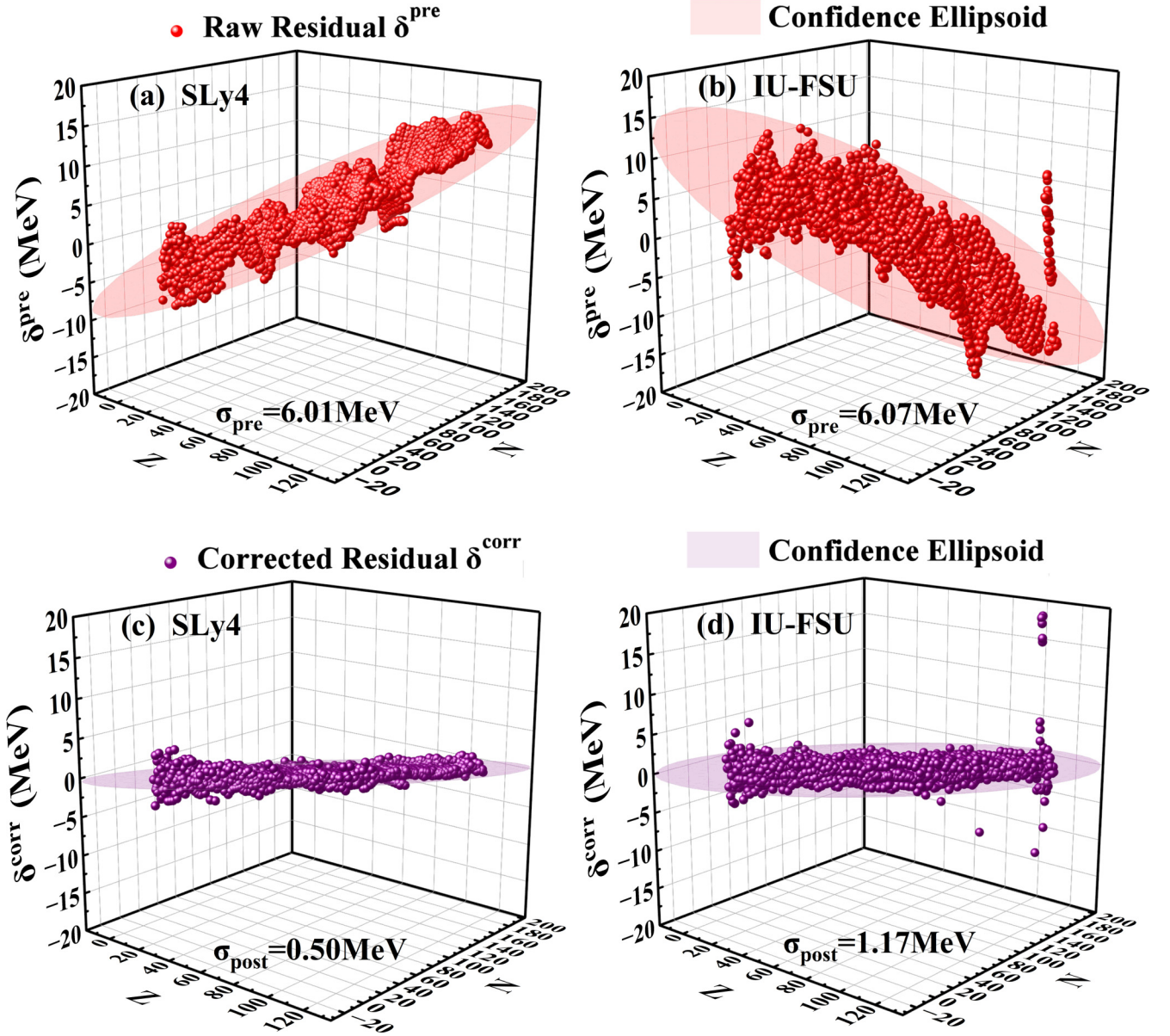


FIG. 2. The distribution of  $\delta^{\text{pre}}$  (red dots) and  $\delta^{\text{corr}}$  (purple dots) for 3471 nuclei in AME2020 from the HFB model with SLy4 parameter set and the RMF model with IU-FSU parameter set. (a) The  $\delta^{\text{pre}}$  of SLy4 parameter set. (b) The  $\delta^{\text{pre}}$  of IU-FSU parameter set. (c) The  $\delta^{\text{corr}}$  of SLy4 parameter set. (d) The  $\delta^{\text{corr}}$  of IU-FSU parameter set.

the values of the  $\sigma_{\text{pre}}$ . Distinct theoretical models exhibit unique characteristics in the  $\delta^{\text{pre}}$  distribution, consequently influencing performance in the calibration of machine learning algorithms. To further elucidate this phenomenon, Fig. 2 displays the raw residuals  $\delta^{\text{pre}}$  and the corrected residuals  $\delta^{\text{corr}}$  from SLy4 and IU-FSU parameter sets. The 95% confidence ellipsoids are presented in the shaded regions. The  $\sigma_{\text{pre}}$  for both the SLy4 and IU-FSU models are approximately 6 MeV, but  $\sigma_{\text{post}}$  exhibit significant disparities. This can be attributed to the distributing characteristic of the  $\delta^{\text{pre}}$ . In Fig. 2(a), the  $\delta^{\text{pre}}$  of the SLy4 model exhibit pronounced shell effects, which display a discernible pattern of regular distribution. However, the distribution of the  $\delta^{\text{pre}}$  for the IU-FSU model exhibits higher levels of randomness and irregularity in Fig. 2(b). The multivariate Bayesian formula (2) relies significantly on

the regularity of the  $\delta^{\text{pre}}$  distribution. The regular distribution of data in the SLy4 model facilitates the acquisition of information by the CBP classifier, but the relatively random distribution of data in the IU-FSU model hinders the capture of physical characteristics in the CBP classifier. Therefore, the SLy4 and IU-FSU parameter sets with the similar  $\sigma_{\text{pre}}$  yield dissimilar  $\sigma_{\text{post}}$  after the CBP method refinements.

In addition, the distributing characteristics of the  $\delta^{\text{pre}}$  of the NL3\*, NLSH, and TM1 parameter sets are consistent with those of the IU-FSU parameter set in Fig. 2, hence leading to the similar  $\sigma_{\text{post}}$  after the CBP method refinements. The same situation also occurs for SkP and SLy4 parameter sets in the HFB models. It should also be noted that in Fig. 2 the IU-FSU parameter set shows evidently deviated data points in the region between  $Z \geq 110$  and  $N \geq 165$ , resulting in higher

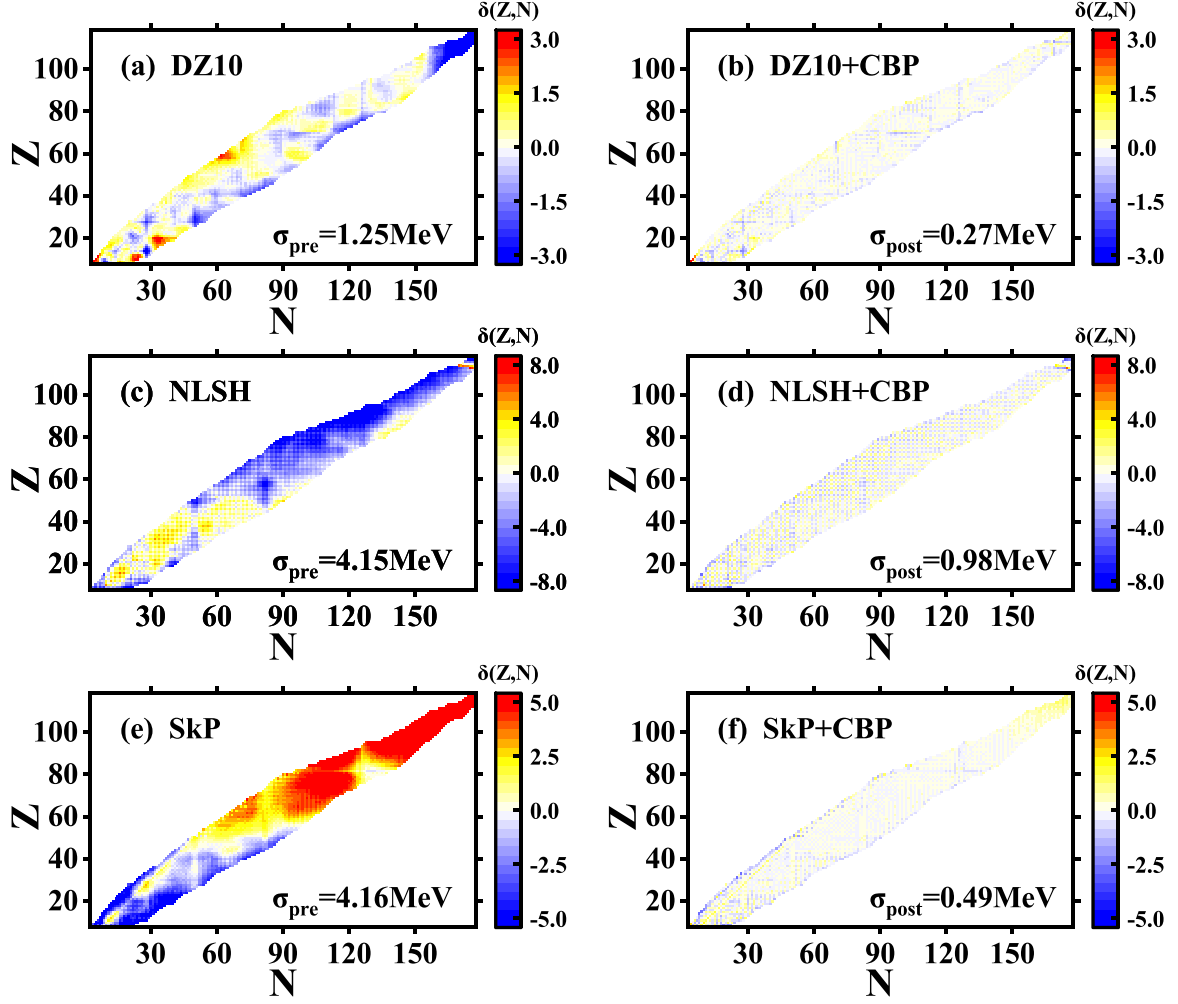


FIG. 3. Left panels: Raw residuals  $\delta^{\text{pre}}$  of the theoretical nuclear masses for the DZ10 model, the RMF model with NLSH parameter set, and the HFB model with SkP parameter set, which includes 3471 nuclei in AME2020. Right panels: The corresponding corrected residuals  $\delta^{\text{corr}}$  by the CBP method. The values of the standard deviations before and after the CBP refinements on the entire set are also presented in the figure.

$\sigma_{\text{pre}}$ . If these deviated data points can be corrected, the raw standard deviation  $\sigma_{\text{pre}}$  will get more reasonable results. Recently, some successful RMF mass tables are proposed, such as the theory with PC-PK1 density functional for even-even nuclei in Refs. [81,82].

To visually demonstrate the efficacy of the CBP method in refining the prediction of mass, we show the comparison of the  $\sigma_{\text{pre}}$  and the  $\sigma_{\text{post}}$  of 3471 nuclei in Fig. 3. The left panels depict the  $\sigma_{\text{pre}}$ , and the right panels illustrate the corresponding  $\sigma_{\text{post}}$  from the CBP method. It is clearly seen that the CBP method has made satisfactory improvements in the accuracy of nuclear mass predictions, especially in the regions of heavy nuclei and the nuclei near the drip line.

### B. Extrapolating capabilities of the CBP method

In this section, we explore the extrapolating capabilities of the CBP method. The entire set of 3471 nuclei with  $Z \geq 8$  is partitioned into the learning set and the validation set. The learning set comprises 3007 nuclei in the AME2003,

and the validation set consists of 464 newly added nuclei in the AME2020. We apply the CBP method to predict the nuclei in the validation set using the prior and conditional probabilities obtained from the data in the learning set. The kernel widths  $h_\delta$ ,  $h_Z$ , and  $h_N$  utilized in the operations of extrapolation correspond to the values previously computed in the section on global optimizations. Table II displays the  $\sigma_{\text{pre}}$  of the theoretical models, the corresponding  $\sigma_{\text{post}}$  after CBP refinements, and the respective  $\Delta\sigma/\sigma_{\text{pre}}$ .

The CBP method produces significant refinements in standard deviations for both the learning and validation sets. First, we assess the extrapolating capability of the CBP method based on the semiempirical formulas. Regarding the DZ10 model, the standard deviations  $\sigma_{\text{pre}}$  in the learning set and the validation set are 1.08 and 2.03 MeV, which indicates the robust extrapolating capability of the DZ10 model. Then we employ the CBP method on the validation set to make predictions. For the DZ10 model, the accuracy of the predictions for the validation sets improves by about 70%. For the WS\* model, we obtain a 50% reduction in the standard deviation.

TABLE II. The raw standard deviation  $\sigma_{\text{pre}}$  (MeV) from the theoretical models and the standard deviation  $\sigma_{\text{post}}$  after the CBP method refinements. The learning set includes 3007 nuclei with  $Z \geq 8$  in the AME2003 compilation, and the validation set includes the 464 newly added nuclei in the AME2020 compilation.

Methods		HFB		RMF				Semiempirical		
		SkP	SLy4	IU-FSU	NL3*	NLSH	TM1	WS*	DZ10	FRDM
Learning set	$\sigma_{\text{pre}}$	4.08	5.81	5.97	2.67	4.05	4.47	0.52	1.08	0.87
	$\sigma_{\text{post}}$	0.42	0.45	1.02	0.92	0.95	1.01	0.30	0.26	0.26
	$\Delta\sigma/\sigma_{\text{pre}}$	90%	92%	83%	65%	77%	77%	42%	76%	70%
Validation set	$\sigma_{\text{pre}}$	4.65	7.19	6.64	4.06	4.76	5.83	0.96	2.03	1.55
	$\sigma_{\text{post}}$	1.06	1.23	2.71	1.61	1.58	1.70	0.48	0.58	0.51
	$\Delta\sigma/\sigma_{\text{pre}}$	77%	83%	59%	60%	67%	71%	50%	72%	67%

For the FRDM model, the standard deviations of validation sets are improved by about 70%. Overall, compared to the improvement in the learning set, the CBP method exhibits reliable extrapolating capabilities.

Besides the semiempirical formulas, the extrapolating capabilities of the CBP method are also discussed based on the HFB models and the RMF models. Regarding the HFB model with SkP parameter set, for the learning set the raw standard deviation  $\sigma_{\text{pre}} = 4.08$  MeV, and for the validation set  $\sigma_{\text{pre}} = 4.65$  MeV, which illustrates the extrapolating capability of HFB models. With the CBP refinements, the standard deviations of the validation set have improved by 77%. For the RMF models with the IU-FSU parameter set, the deviation  $\sigma_{\text{pre}}$  in the learning set is 5.97 MeV, and the deviation  $\sigma_{\text{pre}}$  is 6.64 MeV for the validation set. This indicates that the RMF model has the extrapolating ability. After applying the CBP method to the RMF models, the accuracy of the predictions for the validation sets improves by about 60%. It can be seen from Table II that the  $\sigma_{\text{post}}$  for the validation set is greater than that of the learning set. This is attributed to the nuclei in the validation set being mostly at the edge of the nuclide chart. The nuclei in the validation set are unable to find a large number of identical  $Z$  and  $N$  in the learning set, reducing the precision of the  $\delta^{\text{corr}}$ . The accuracy of the CBP method will improve as the masses of more exotic nuclei are accurately measured.

The results in Table II illustrate that the CBP method exhibits strong extrapolating ability. The reason has mainly two aspects. On the one hand, theoretical mass models based on nuclear interactions can clearly capture the primary physical essence. This helps to describe the general trend of the changes in nuclear mass. On the other hand, the CBP method can detect finer structures and unknown physical effects within nuclei. The grasp of details allows CBP to fine tune the results of the theoretical mass models. From Tables I and II, both global and extrapolated results show satisfactory improvements in the description of the nuclear mass. Thus,

we can use the CBP method to make reliable predictions for regions lacking experimental data.

### C. Further refinement employing the BMA method

The mass models after the CBP refinements exhibit favorable predictive performance on the nucleus near the  $\beta$ -stability line. In the vicinity of the drip line, each category of theoretical models shows optimal predictive performance within specific regions. Therefore, it is necessary to comprehensively consider the strengths of various models through the BMA method. By assigning weights through benchmark nuclei, the BMA method balances the anticipated discrepancies between several theoretical models based on the entire nuclide chart. To assess the reliability of the BMA method, we predict the neutron drip line using Ca isotopes as an example.

First, we predict the masses of seven benchmark nuclei:  $^{19}\text{Mg}$  [73],  $^{54}\text{Sc}$  [74],  $^{67}\text{Kr}$  [75],  $^{80}\text{Zr}$  [4],  $^{112}\text{Mo}$  [76],  $^{127}\text{La}$  [77], and  $^{153}\text{Pm}$  [78], using different theoretical models based on the 3007 nuclear data from the learning set. The masses of these seven benchmark nuclei have been recently measured [71], covering the entire range from the light to heavy nuclei regions and from the neutron-rich to proton-rich regions of the nuclide chart. Then we obtain the corrected mass residuals  $\delta^{\text{corr}} = E^{\text{exp}} - E^{\text{corr}}$  of these benchmark nuclei. The predictive ability  $P(D|M_k)$  of each model is assessed by constructing the Gaussian distribution according to Eq. (15). By utilizing the  $P(D|M_k)$  as the evaluation criterion, the weight  $P(M_k|D)$  is given for each model by the Bayesian formula Eq. (14). Selecting benchmark nuclei from different regions impacts the allocation of weights in the BMA method. The weights of all candidate models are displayed in Table III.

In Table III, we can see that the BMA method assigns different weights to various models. It can be explained by Fig. 4, which shows the  $\delta^{\text{corr}}$  of all the seven target nuclei. The error bars for the nine mass models are calculated using the one-sigma uncertainty  $\sigma^{\text{em}}(Z, N)$  from Eq. (18), and the error

TABLE III. The weights of nine mass models by BMA are based on the refined residuals of seven target nuclei in all regions:  $^{19}\text{Mg}$ ,  $^{54}\text{Sc}$ ,  $^{67}\text{Kr}$ ,  $^{80}\text{Zr}$ ,  $^{112}\text{Mo}$ ,  $^{127}\text{La}$ , and  $^{153}\text{Pm}$ .

Models	SkP	SLy4	IU-FSU	NL3*	NLSH	TM1	WS*	DZ10	FRDM
Weight	0.03	0.13	0.05	0.02	0.08	0.03	0.36	0.19	0.10

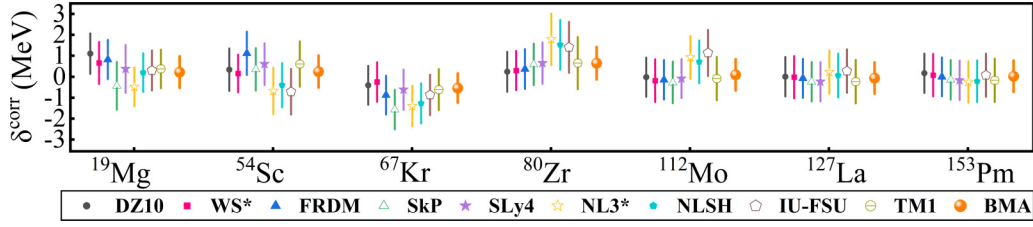


FIG. 4. The corrected residuals  $\delta^{\text{corr}}$  along with error bars for seven target nuclei:  $^{19}\text{Mg}$ ,  $^{54}\text{Sc}$ ,  $^{67}\text{Kr}$ ,  $^{80}\text{Zr}$ ,  $^{112}\text{Mo}$ ,  $^{127}\text{La}$ , and  $^{153}\text{Pm}$ . The results of nine theoretical models refined by the CBP method and the results of the BMA are listed.

bars for the model averaging results BMA are determined using the uncertainty of BMA  $\sigma^{\text{BMA}}(Z, N)$  from Eq. (19). The WS\* and DZ10 models are assigned higher weights because they provide smaller deviations from experimental data. The SLy4, NLSH, and FRDM models contribute relatively small weights of around 10% due to their unfavorable predictive performance for  $^{54}\text{Sc}$  and  $^{80}\text{Zr}$ , as seen in Fig. 4. The SkP, IU-FSU, NL3\*, and TM1 have weights not exceeding 5% because their predictions for  $^{19}\text{Mg}$ ,  $^{54}\text{Sc}$ ,  $^{67}\text{Kr}$ ,  $^{80}\text{Zr}$ , and  $^{112}\text{Mo}$  show apparent deviations from the experimental data. Comparable arguments also be discussed in Ref. [61].

Then we can obtain the combined predictive result of the nucleus  $(Z_i, N_i)$  by Eq. (16). The combined deviation  $\sigma_{\text{BMA}}$  for 464 nuclei in the validation set is 0.430 MeV, which is smaller than the standard deviations  $\sigma_{\text{post}}$  of all nine theoretical models in Table II. This shows that the BMA method can effectively extract the advantages of different nuclear models and obtain more accurate results of prediction.

As a followup to the previous discussions, we utilize the BMA method to predict the neutron drip line of the Ca isotopes. In Fig. 5, we present the extrapolated one-neutron

separation energies  $S_{1n}$  of the odd- $N$  isotopes and two-neutron separation energies  $S_{2n}$  of even- $N$  isotopes. The solid lines show the average prediction by BMA, while the shaded bands represent the associated one-sigma uncertainty  $\sigma^{\text{BMA}}(Z, N)$  in Eq. (19). Due to the pairing effects of nucleons, it can be observed in Fig. 5 that the one-neutron drip line reaches zero earlier than the two-neutron drip line. Since nuclei with negative separation energies are particle unstable, the extrapolated separation energy can be used to determine the existence probability of nuclei. We define the posterior probability of existence as  $P_{\text{ex}}(Z, N) = P(S_{1n/2n}^*(Z, N) > 0 | S_{1n/2n})$ , which denotes the proportions of the positive separation energies relative to the total range of errors. The results are presented in the inset. For the heaviest discovered Ca isotope  $^{60}\text{Ca}$ , the predicted probability of existence is  $P_{\text{ex}}(20, 40) = 1.0$ , which indicates the definite existence of this nucleus. The probability of the existence of  $^{60}\text{Ca}$  by the BMA method is in agreement with the experimental measurements in Ref. [71].

Furthermore, the posterior predicted results of the BMA method place the  $1n$  drip line for Ca around  $^{71}\text{Ca}$  and the  $2n$  drip line around  $^{72}\text{Ca}$ . In this study, seven benchmark nuclei from diverse regions are adopted, and the probabilities of existence are  $P_{\text{ex}}(20, 51) = 0.03$  and  $P_{\text{ex}}(20, 52) = 0.10$ . The region of benchmark nuclei influences the predictive outcomes of the BMA method, resulting in slight variations in the predictions for the drip line. In the recent research [59], they selected three neutron-rich nuclei,  $^{49}\text{S}$ ,  $^{52}\text{Cl}$ , and  $^{53}\text{Ar}$ , as benchmark nuclei to predict the neutron drip line of the Ca isotopes. Fig. 5 presents predictions consistent with those in Ref. [59].

#### IV. SUMMARY

In this paper, we refined the nine theoretical nuclear mass models by combining the continuous Bayesian probability (CBP) method and the Bayesian model average (BMA) method. There are two main innovations. On the one hand, the CBP method introduces continuous probability density functions to enable a thorough exploration of the local mass relations of the nuclei with the same  $Z$  and  $N$ . On the other hand, the BMA method comprehensively considers the predictive performance of different theoretical models for nuclei in the entire nuclide chart, which leads to a more accurate prediction for nuclear masses.

The effectiveness of the CBP method is demonstrated in global optimizations and extrapolation analyses. For the global optimizations, the CBP method exhibits an improve-

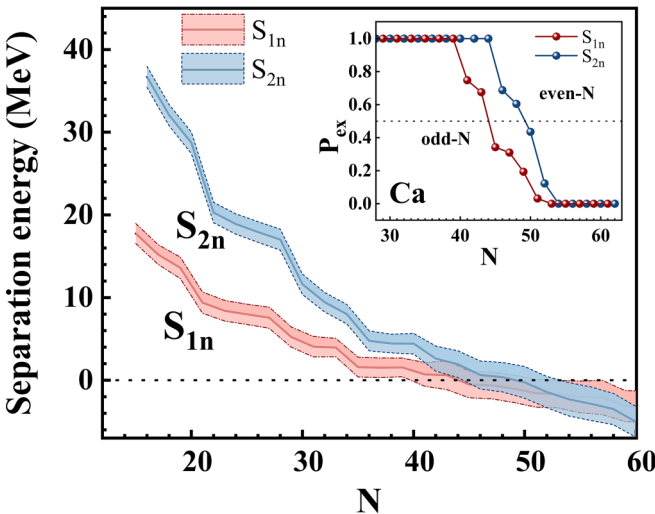


FIG. 5. The extrapolations with the BMA method for one-neutron separation energy  $S_{1n}$  of the odd- $N$  Ca isotopes and two-neutron separation energy  $S_{2n}$  of the even- $N$  Ca isotopes. The solid lines denote the average prediction by the BMA method, while the shaded bands represent the associated uncertainty  $\sigma^{\text{BMA}}(Z, N)$ . The inset shows the probability of the existence for the Ca chain. The limit of zero separation energy and the  $P_{\text{ex}} = 0.5$  limit are indicated by dotted lines.



ment of around 90% for the HFB models, 80% for the RMF models, and over 60% for the semi-empirical formulas. For the extrapolating capabilities, the accuracy of the predictions in the validation sets improves by about 80% for the HFB models, 70% for the RMF models, and 50% for the semiempirical formulas. In addition, we employ the BMA method to assign weight to the predictive performance of each model, which is indicated by the corrected mass residuals of seven benchmark nuclei. Distinct theoretical models exhibit different predictive performances within certain regions. The region of benchmark nuclei impacts the predictive results of the BMA method. In order to assess the reliability of BMA, we predict the neutron drip line of the Ca isotopic by presenting the extrapolation for one-neutron (two-neutron) separation energy  $S_{1n}$  ( $S_{2n}$ ), which is consistent with the experimental data.

Generally, with the application of the CBP and BMA methods, the description of the nuclear masses is significantly

improved. Theoretical nuclear models convincingly describe the principal changing trends of nuclear masses, and CBP combined with the BMA method provides reliable refinements. Our analysis indicates that the CBP and BMA methods can provide support for predicting masses of exotic nuclei near the drip line, and can be used in other nuclear studies such as nuclear charge radii, nuclear reactions, and nuclear decay.

## ACKNOWLEDGMENTS

This work was supported by the National Natural Science Foundation of China (Grants No. 11505292, No. 11822503, No. 11975167, and No. 12035011), by the Shandong Provincial Natural Science Foundation, China (Grant No. ZR2020MA096), and by the Fundamental Research Funds for the Central Universities (Grant No. 22CX03017A).

- 
- [1] D. Lunney, J. M. Pearson, and C. Thibault, *Rev. Mod. Phys.* **75**, 1021 (2003).
  - [2] S. R. Stroberg, A. Calci, H. Hergert, J. D. Holt, S. K. Bogner, R. Roth, and A. Schwenk, *Phys. Rev. Lett.* **118**, 032502 (2017).
  - [3] M. Bender, P.-H. Heenen, and P.-G. Reinhard, *Rev. Mod. Phys.* **75**, 121 (2003).
  - [4] A. Hamaker, E. Leistenschneider, R. Jain, G. Bollen, S. Giuliani, K. Lund, W. Nazarewicz, L. Neufcourt, C. Nicoloff, D. Puentes *et al.*, *Nat. Phys.* **17**, 1408 (2021).
  - [5] J. Giovannazzo, B. Blank, M. Chartier, S. Czajkowski, A. Fleury, M. J. Lopez Jimenez, M. S. Pravikoff, J.-C. Thomas, F. de Oliveira Santos, M. Lewitowicz, V. Maslov, M. Stanoiu, R. Grzywacz, M. Pfützner, C. Borcea, and B. A. Brown, *Phys. Rev. Lett.* **89**, 102501 (2002).
  - [6] Z. M. Niu, H. Z. Liang, B. H. Sun, W. H. Long, and Y. F. Niu, *Phys. Rev. C* **99**, 064307 (2019).
  - [7] K. Auranen, D. Seweryniak, M. Albers, A. D. Ayangeakaa, S. Bottoni, M. P. Carpenter, C. J. Chiara, P. Copp, H. M. David, D. T. Doherty, J. Harker, C. R. Hoffman, R. V. F. Janssens, T. L. Khoo, S. A. Kuvin, T. Lauritsen, G. Lotay, A. M. Rogers, J. Sethi, C. Scholey *et al.*, *Phys. Rev. Lett.* **121**, 182501 (2018).
  - [8] P. Möller, D. Madland, A. Sierk, and A. Iwamoto, *Nature (London)* **409**, 785 (2001).
  - [9] S. Panebianco, J.-L. Sida, H. Goutte, J.-F. Lemaître, N. Dubray, and S. Hilaire, *Phys. Rev. C* **86**, 064601 (2012).
  - [10] Y. T. Oganessian and V. K. Utyonkov, *Rep. Prog. Phys.* **78**, 036301 (2015).
  - [11] Y. Oganessian and V. Utyonkov, *Nucl. Phys. A* **944**, 62 (2015).
  - [12] D. Martin, A. Arcones, W. Nazarewicz, and E. Olsen, *Phys. Rev. Lett.* **116**, 121101 (2016).
  - [13] B. Sun, Y. A. Litvinov, I. Tanihata, and Y. Zhang, *Front. Phys.* **10**, 1 (2015).
  - [14] W. F. Henning, *Nucl. Instrum. Methods Phys. Res., Sect. B* **214**, 211 (2004).
  - [15] M. Wang, Y. H. Zhang, X. Zhou, X. H. Zhou, H. S. Xu, M. L. Liu, J. G. Li, Y. F. Niu, W. J. Huang, Q. Yuan, S. Zhang, F. R. Xu, Y. A. Litvinov, K. Blaum, Z. Meisel, R. F. Casten, R. B. Cakirli, R. J. Chen, H. Y. Deng, C. Y. Fu *et al.*, *Phys. Rev. Lett.* **130**, 192501 (2023).
  - [16] X. Zhou, M. Wang, Y. Zhang, Y. A. Litvinov, Z. Meisel, K. Blaum, X. Zhou, S. Hou, K. Li, H. Xu *et al.*, *Nat. Phys.* **19**, 1091 (2023).
  - [17] W. Kutschera, A. J. T. Jull, M. Paul, and A. Wallner, *Rev. Mod. Phys.* **95**, 035006 (2023).
  - [18] R. Kalpakchieva, H. Bohlen, W. Von Oertzen, B. Gebauer, M. von Lucke-Petsch, T. Massey, A. Ostrowski, T. Stolla, M. Wilpert, and T. Wilpert, *Eur. Phys. J. A* **7**, 451 (2000).
  - [19] X. L. Tu, H. S. Xu, M. Wang, Y. H. Zhang, Y. A. Litvinov, Y. Sun, H. Schatz, X. H. Zhou, Y. J. Yuan, J. W. Xia, G. Audi, K. Blaum, C. M. Du, P. Geng, Z. G. Hu, W. X. Huang, S. L. Jin, L. X. Liu, Y. Liu, X. Ma *et al.*, *Phys. Rev. Lett.* **106**, 112501 (2011).
  - [20] J. Erler, N. Birge, M. Kortelainen, W. Nazarewicz, E. Olsen, A. M. Perhac, and M. Stoitsov, *Nature (London)* **486**, 509 (2012).
  - [21] S. E. Agbemava, A. V. Afanasjev, D. Ray, and P. Ring, *Phys. Rev. C* **89**, 054320 (2014).
  - [22] W. Nazarewicz, *Nat. Phys.* **14**, 537 (2018).
  - [23] S. Goriely, N. Chamel, and J. M. Pearson, *Phys. Rev. C* **93**, 034337 (2016).
  - [24] L. Wang, Q. Niu, J. Zhang, J. Liu, and Z. Ren, *Sci. China Phys. Mech. Astron.* **66**, 102011 (2023).
  - [25] N. Schunck, J. Dobaczewski, J. McDonnell, J. Moré, W. Nazarewicz, J. Sarich, and M. V. Stoitsov, *Phys. Rev. C* **81**, 024316 (2010).
  - [26] J. C. Pei, A. T. Kruppa, and W. Nazarewicz, *Phys. Rev. C* **84**, 024311 (2011).
  - [27] M. V. Stoitsov, J. Dobaczewski, P. Ring, and S. Pittel, *Phys. Rev. C* **61**, 034311 (2000).
  - [28] K. Zhang, M.-K. Cheoun, Y.-B. Choi, P. S. Chong, J. Dong, Z. Dong, X. Du, L. Geng, E. Ha, X.-T. He, C. Heo, M. C. Ho, E. J. In, S. Kim, Y. Kim, C.-H. Lee, J. Lee, H. Li, Z. Li, T. Luo *et al.*, *At. Data Nucl. Data Tables* **144**, 101488 (2022).
  - [29] J. Dobaczewski, H. Flocard, and J. Treiner, *Nucl. Phys. A* **422**, 103 (1984).

- [30] E. Chabanat, P. Bonche, P. Haensel, J. Meyer, and R. Schaeffer, *Nucl. Phys. A* **635**, 231 (1998).
- [31] L. Wang, J. Liu, R. Wang, M. Lyu, C. Xu, and Z. Ren, *Phys. Rev. C* **103**, 054307 (2021).
- [32] W. Pannert, P. Ring, and J. Boguta, *Phys. Rev. Lett.* **59**, 2420 (1987).
- [33] J. Liu, R. Xu, J. Zhang, C. Xu, and Z. Ren, *J. Phys. G* **46**, 055105 (2019).
- [34] W.-C. Chen and J. Piekarewicz, *Phys. Rev. C* **90**, 044305 (2014).
- [35] L. Geng, H. Toki, and J. Meng, *Prog. Theor. Phys.* **113**, 785 (2005).
- [36] J. Liu, Y. Wang, Y. Gao, P. Danielewicz, C. Xu, and Z. Ren, *Phys. Rev. C* **106**, 054605 (2022).
- [37] H. Wang, Q. Su, C. Xu, Z. Ren, and J. Liu, *J. Phys. G: Nucl. Part. Phys.* **50**, 095104 (2023).
- [38] J. Liu, X. Liu, X. Wang, S. Wang, C. Xu, and Z. Ren, *J. Phys. G: Nucl. Part. Phys.* **48**, 125105 (2021).
- [39] F. J. Fattoyev, C. J. Horowitz, J. Piekarewicz, and G. Shen, *Phys. Rev. C* **82**, 055803 (2010).
- [40] G. Lalazissis, S. Karatzikos, R. Fossion, D. P. Arteaga, A. Afanasjev, and P. Ring, *Phys. Lett. B* **671**, 36 (2009).
- [41] M. Sharma, M. Nagarajan, and P. Ring, *Phys. Lett. B* **312**, 377 (1993).
- [42] Y. Sugahara and H. Toki, *Nucl. Phys. A* **579**, 557 (1994).
- [43] N. Wang, M. Liu, X. Wu, and J. Meng, *Phys. Lett. B* **734**, 215 (2014).
- [44] N. Wang, M. Liu, L. Ou, and Y. Zhang, *Phys. Lett. B* **751**, 553 (2015).
- [45] J. Duflo and A. P. Zuker, *Phys. Rev. C* **52**, R23(R) (1995).
- [46] J. Mendoza-Temis, J. G. Hirsch, and A. P. Zuker, *Nucl. Phys. A* **843**, 14 (2010).
- [47] P. Möller, A. Sierk, T. Ichikawa, and H. Sagawa, *At. Data Nucl. Data Tables* **109-110**, 1 (2016).
- [48] P. Möller, A. J. Sierk, T. Ichikawa, and H. Sagawa, *At. Data Nucl. Data Tables* **59**, 185 (1995).
- [49] M. R. Mumpower, T. M. Sprouse, A. E. Lovell, and A. T. Mohan, *Phys. Rev. C* **106**, L021301 (2022).
- [50] Z.-P. Gao, Y.-J. Wang, H.-L. Lü, Q.-F. Li, C.-W. Shen, and L. Liu, *Nucl. Sci. Tech.* **32**, 109 (2021).
- [51] W. He, Q. Li, Y. Ma, Z. Niu, J. Pei, and Y. Zhang, *Sci. China Phys. Mech. Astron.* **66**, 282001 (2023).
- [52] I. Vidaña, *Nucl. Phys. A* **1032**, 122625 (2023).
- [53] X.-K. Du, P. Guo, X.-H. Wu, and S.-Q. Zhang, *Chin. Phys. C* **47**, 074108 (2023).
- [54] T. C. Yiu, H. Liang, and J. Lee, *Chin. Phys. C* **48**, 024102 (2024).
- [55] X. Wu, Y. Lu, and P. Zhao, *Phys. Lett. B* **834**, 137394 (2022).
- [56] T.-L. Zhao and H.-F. Zhang, *Chin. Phys. C* **46**, 044103 (2022).
- [57] R. Utama, J. Piekarewicz, and H. B. Prosper, *Phys. Rev. C* **93**, 014311 (2016).
- [58] R. Utama and J. Piekarewicz, *Phys. Rev. C* **96**, 044308 (2017).
- [59] L. Neufcourt, Y. Cao, W. Nazarewicz, E. Olsen, and F. Viens, *Phys. Rev. Lett.* **122**, 062502 (2019).
- [60] L. Neufcourt, Y. Cao, S. A. Giuliani, W. Nazarewicz, E. Olsen, and O. B. Tarasov, *Phys. Rev. C* **101**, 044307 (2020).
- [61] L. Neufcourt, Y. Cao, S. Giuliani, W. Nazarewicz, E. Olsen, and O. B. Tarasov, *Phys. Rev. C* **101**, 014319 (2020).
- [62] Y. Ma, C. Su, J. Liu, Z. Ren, C. Xu, and Y. Gao, *Phys. Rev. C* **101**, 014304 (2020).
- [63] Y. Liu, C. Su, J. Liu, P. Danielewicz, C. Xu, and Z. Ren, *Phys. Rev. C* **104**, 014315 (2021).
- [64] D. Bowser-Chao and D. L. Dzialo, *Phys. Rev. D* **47**, 1900 (1993).
- [65] W. S. Noble, *Nat. Biotechnol.* **24**, 1565 (2006).
- [66] F.-D. Qin, H.-Y. Luo, Z.-Z. He, K.-J. Lu, C.-G. Wang, M.-M. Wu, Z.-K. Fan, and J. Shan, *Nucl. Sci. Tech.* **34**, 37 (2023).
- [67] D. Wu, C. L. Bai, H. Sagawa, S. Nishimura, and H. Q. Zhang, *Phys. Rev. C* **104**, 054303 (2021).
- [68] J. Gordon and J. M. Hernández-Lobato, *Pattern Recognit.* **100**, 107156 (2020).
- [69] Z. Jin, M. Yan, H. Zhou, A. Cheng, Z. Ren, and J. Liu, *Phys. Rev. C* **108**, 014326 (2023).
- [70] W. I. Jay and E. T. Neil, *Phys. Rev. D* **103**, 114502 (2021).
- [71] M. Wang, W. Huang, F. Kondev, G. Audi, and S. Naimi, *Chin. Phys. C* **45**, 030003 (2021).
- [72] G. Audi, A. Wapstra, and C. Thibault, *Nucl. Phys. A* **729**, 337 (2003).
- [73] H. T. Fortune and R. Sherr, *Phys. Rev. C* **85**, 051302(R) (2012).
- [74] E. Leistenschneider, E. Dunling, G. Bollen, B. A. Brown, J. Dilling, A. Hamaker, J. D. Holt, A. Jacobs, A. A. Kwiatkowski, T. Miyagi, W. S. Porter, D. Puentes, M. Redshaw, M. P. Reiter, R. Ringle, R. Sandler, C. S. Sumithrarachchi, A. A. Valverde, and I. T. Yandow (The LEBIT Collaboration and the TITAN Collaboration), *Phys. Rev. Lett.* **126**, 042501 (2021).
- [75] Z. Zhang, C. Yuan, C. Qi, B. Cai, and X. Xu, *Phys. Lett. B* **838**, 137740 (2023).
- [76] D. S. Hou, A. Takamine, M. Rosenbusch, W. D. Xian, S. Iimura, S. D. Chen, M. Wada, H. Ishiyama, P. Schury, Z. M. Niu, H. Z. Liang, S. X. Yan, P. Doornenbal, Y. Hirayama, Y. Ito, S. Kimura, T. M. Kojima, W. Korten, J. Lee, J. J. Liu *et al.*, *Phys. Rev. C* **108**, 054312 (2023).
- [77] B. Saygı, *Nucl. Phys. A* **983**, 223 (2019).
- [78] V. Rani, P. Verma, S. Singh, M. Rajput, A. Bharti, G. H. Bhat, and J. A. Sheikh, *Chin. Phys. C* **44**, 094107 (2020).
- [79] M. Stoitsov, N. Schunck, M. Kortelainen, N. Michel, H. Nam, E. Olsen, J. Sarich, and S. Wild, *Comput. Phys. Commun.* **184**, 1592 (2013).
- [80] P. Ring, Y. Gambhir, and G. Lalazissis, *Comput. Phys. Commun.* **105**, 77 (1997).
- [81] Y. L. Yang, Y. K. Wang, P. W. Zhao, and Z. P. Li, *Phys. Rev. C* **104**, 054312 (2021).
- [82] <http://nuclearmap.jcnp.org/index.html>.